

Computational simulations of hemodynamic changes within thoracic, coronary, and cerebral arteries following early wall remodeling in response to distal aortic coarctation

Jessica S. Coogan · Jay D. Humphrey ·
C. Alberto Figueroa

Received: 3 August 2011 / Accepted: 23 February 2012
© Springer-Verlag 2012

Abstract Mounting evidence suggests that the pulsatile character of blood pressure and flow within large arteries plays a particularly important role as a mechano-biological stimulus for wall growth and remodeling. Nevertheless, understanding better the highly coupled interactions between evolving wall geometry, structure, and properties and the hemodynamics will require significantly more experimental data. Computational fluid–solid–growth models promise to aid in the design and interpretation of such experiments and to identify candidate mechanobiological mechanisms for the observed arterial adaptations. Motivated by recent aortic coarctation models in animals, we used a computational fluid–solid interaction model to study possible local and systemic effects on the hemodynamics within the thoracic aorta and coronary, carotid, and cerebral arteries due to a distal aortic coarctation and subsequent spatial variations in wall adaptation. In particular, we studied an initial stage of acute cardiac compensation (i.e., maintenance of cardiac output) followed by early arterial wall remodeling (i.e., spatially varying wall thickening and stiffening). Results suggested, for example, that while coarctation increased both the mean

and pulse pressure in the proximal vessels, the locations nearest to the coarctation experienced the greatest changes in pulse pressure. In addition, after introducing a spatially varying wall adaptation, pressure, left ventricular work, and wave speed all increased. Finally, vessel wall strain similarly experienced spatial variations consistent with the degree of vascular wall adaptation.

Keywords FSI · Arterial adaptation · Aortic banding · Pulse pressure · Hypertension

1 Introduction

Altered blood pressure and flow cause and are caused by changes in the mechanical properties of arteries. These changes begin at the cellular level, with endothelial cells, smooth muscle cells, and adventitial fibroblasts responding to hemodynamically induced alterations in wall shear and intramural stress via altered gene expression (Gibbons and Dzau 1994; Langille 1996; Chien et al. 1998; Humphrey 2008). In hypertension, for example, the smooth muscle cells hypertrophy, proliferate, and synthesize additional extracellular matrix proteins and glycoproteins, which leads to a thickening and stiffening of the wall that appears to return intramural stress toward normal values (Wolinsky 1970; Matsumoto and Hayashi 1994; Laurent et al. 2005). Although elevated mean arterial pressure (MAP) has traditionally been considered to be an important indicator or initiator of cardiovascular risk in hypertension, mounting evidence suggests that increased pulse pressure is as or more important (Safar 2000; Dart and Kingwell 2001; Safar and Boudier 2005). Of particular note, data from surgically created aortic coarctations in animals reveal striking evolutions of wall geometry, structure, and properties (Xu et al. 2000;

J. S. Coogan
Department of Bioengineering, Stanford University,
Stanford, CA, USA

J. D. Humphrey
Department of Biomedical Engineering,
Yale University, New Haven, CT, USA

C. A. Figueroa
Department of Biomedical Engineering,
King's College London, London, UK

C. A. Figueroa (✉)
The Rayne Institute, St Thomas' Hospital, 4th Floor,
London SE1 7EH, UK
e-mail: alberto.figueroa@kcl.ac.uk

Hu et al. 2008; Eberth et al. 2010) that appear to be driven primarily by increased pulse pressure, not MAP (Eberth et al. 2009). It also appears that the associated arterial adaptations progress at different rates and to different extents both temporally (first at basal rates, then rapidly, then back to nearly normal values) and spatially (from proximal to distal sites)—see Hayenga (2010). Although additional experimental data will be needed to understand better these spatio-temporal adaptations, computational fluid–solid–growth models (FSG) (e.g., Figueroa et al. 2009) offer considerable promise both in the design and interpretation of such experiments and in implicating possible biomechanical mechanisms (Humphrey and Taylor 2008).

Computational simulations can reveal detailed information within large segments of the vasculature and thereby can increase our understanding of both local and systemic effects of arterial growth and remodeling (G&R). Whereas many different portions of the vasculature have been modeled previously (e.g., the aorta as well as coronary, pulmonary, and cerebral arterial trees—Humphrey and Taylor 2008; Taylor and Figueroa 2009; LaDisa et al. 2010), recent advances enable more reliable simulations particularly for complex regions such as the thoracic aorta. For example, in many cases there is a need to ensure strong coupling of the heart and vasculature, stabilization of flow at vessel outlets, spatial variations in wall properties, coupling of the arterial wall and perivascular tissue, and effects of distal resistance beds on proximal flows (Figueroa et al. 2006; Vignon-Clementel et al. 2006; Kim et al. 2009a,b; Moireau et al. 2012; Bazilevs et al. 2009a,b; Coogan et al. 2011; LaDisa et al. 2011a,b; Xiong et al. 2011). Building on these and other recent advances, the goal of this work was to simulate possible effects of a surgically created coarctation in the descending thoracic aorta on the hemodynamics within the proximal aorta and the coronary, carotid, and cerebral arteries following both an acute cardiac compensation (i.e., maintenance of cardiac output) and early arterial wall remodeling (i.e., spatially varying wall thickening and stiffening).

2 Methods

2.1 Model geometry

2.1.1 Baseline model

Computed tomographic (CT) images were collected from two adult male human subjects free of cardiovascular disease to collectively encompass all major arteries from the brain to the diaphragm. Two datasets were necessary since healthy individuals do not usually receive full-body CT imaging due to radiation concerns. Imaging for one subject consisted of

cardiac-gated CT angiography encompassing the coronary arteries and thoracic aorta; imaging for the other subject consisted of CT angiography encompassing all major arteries in the head and neck. The cardiac-gated CT angiography consisted of a $512 \times 512 \times 299$ voxel image with a resolution of $0.62 \text{ mm} \times 0.62 \text{ mm} \times 1 \text{ mm}$. The CT angiography of the head and neck consisted of a $512 \times 512 \times 709$ voxel image with a resolution of $0.35 \text{ mm} \times 0.35 \text{ mm} \times 0.5 \text{ mm}$. Separate three-dimensional geometric models were constructed from the two CT datasets using custom software based on a two-dimensional vessel segmentation procedure (Wilson et al. 2001); centerline paths were defined through the vessels of interest and the imaging data were resampled in planes perpendicular to the path. The vessel boundary was either identified using thresholding, which determined boundaries based on differences in pixel intensity, or demarcated interactively by hand. Each three-dimensional model was then created by an automated lofting process that connected, by interpolation, all determined boundaries. The two models were combined by translating the model containing the head and neck vessels until the origin of the arch arteries intersected the aortic arch of the model containing the coronary arteries and thoracic aorta (Fig. 1). There was no need to scale any of the vessels because the neck arteries intersected naturally the aortic arch.

A finite element mesh was created by discretizing the three-dimensional model coarsely, running a steady-state flow simulation, and then performing field-based adaptive mesh refinement (Sahni et al. 2006). This procedure allowed the resulting finite element mesh to capture a broad range of arterial diameters since smaller vessels such as cerebral arteries were discretized with more elements whereas larger vessels such as the thoracic aorta were discretized more coarsely (Fig. 2). The final finite element mesh consisted of 2,462,487 linear tetrahedral elements and 477,872 nodes.

2.1.2 Coarctation model

A thoracic aortic coarctation was modeled by introducing a narrowing in the aorta just above the diaphragm, consistent with both the location and the degree of a surgically induced coarctation in mini-pigs in studies that provide information on temporal and spatial changes in arterial wall composition (Hu et al. 2008; Hayenga 2010). This narrowing was created by scaling the original segmented vessel cross-sections to create a 75% reduction in diameter relative to the normal aortic diameter proximal to the location of the narrowing.

2.2 Numerical methods

Equations enforcing balance of mass and linear momentum (Navier–Stokes) were solved for the flow of an incompressible Newtonian fluid within a deformable domain using

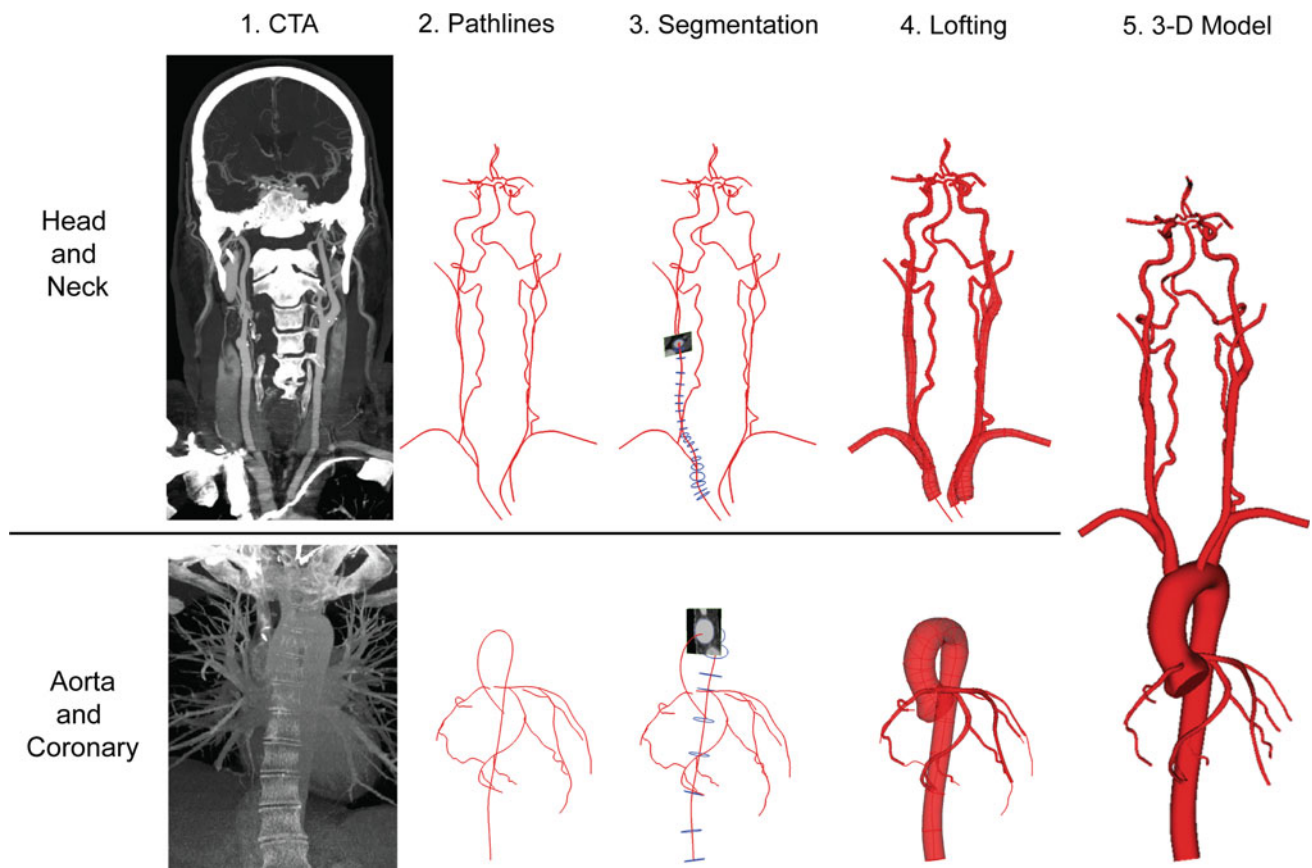


Fig. 1 Schematic of the process for generating the final three-dimensional computational model of the human thoracic aorta, coronary arteries, and head and neck vessels based on CT images from two normal male subjects

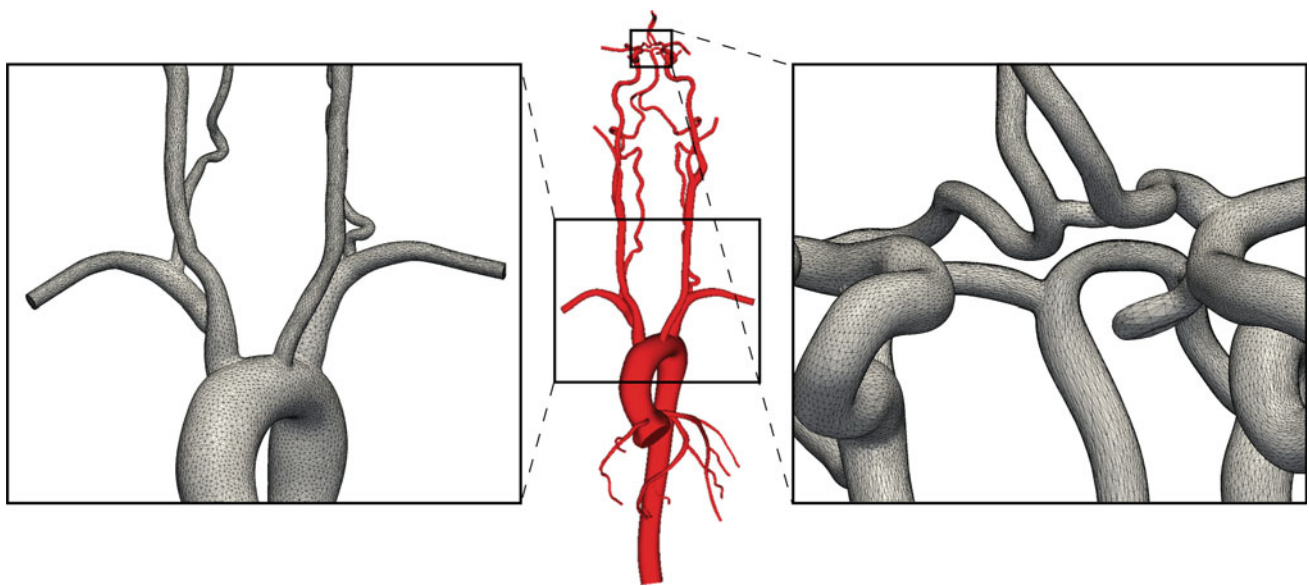


Fig. 2 Close-up view of the finite element mesh in the aortic arch (*left*) and circle of Willis (*right*). Field-based adaptive mesh refinement techniques facilitated adequate resolution throughout the computational domain while keeping a reasonable bound on the final mesh size

a stabilized finite element formulation implemented in the open-source code SimVascular (Whiting and Jansen 2001; Figueroa et al. 2006; <http://wiki.simtk.org/simvascular/>).

Computations were performed on a supercomputer with 2,208 cores (276 Dell PowerEdge 1950 computer nodes, consisting of dual-socket quad-core processors, with 16 GB of

memory each), typically using 96 cores. Based on pilot studies, we utilized a time step size of 0.0001 s, and the simulations had an average residual of 0.005. Simulations were run for 7 cardiac cycles until achieving cycle-to-cycle periodicity in the pressure fields, which typically required a runtime of 10 days. The only observed cycle-to-cycle variations in the flow field were at the outlet of the aorta, as expected due to the complex transitional flow generated at the coarctation. All reported results correspond to the seventh cycle.

2.3 Fluid–solid models

Blood density was $\rho = 1.06 \text{ kg/m}^3$ and blood viscosity was $\mu = 0.04 \text{ P}$. As noted below, we similarly assumed typical baseline values for the linearized stiffness and thickness of the wall of each of the four primary vascular segments: thoracic aorta as well as coronary, neck, and cerebral arteries. A coupled momentum method (Figuerao et al. 2006) was used to model wall deformability and a coupled-multidomain formulation (Vignon-Clementel et al. 2006) was used to link lumped parameter models for the heart and distal vessels (i.e., Windkessel models) to the three-dimensional vascular model. The overall model thus required prescription of one inlet and 22 outlet boundary conditions. Numerical values for the lumped parameter coefficients were determined iteratively to reach target values for flow and pressure (see below).

2.3.1 Heart model

Overall function of the heart was simulated using a lumped parameter circuit model (Kim et al. 2009b) that includes resistors and inductors to represent the mitral and aortic valves (R_{AV} , R_{V-Art} , L_{AV} , L_{V-Art}), a pressure source that represents left atrial pressure (P_{LA}), and a variable capacitance that represents left ventricular elastance/contractility ($E(t)$)—see Fig. 3. Values of the resistances and inductances were obtained from a previous circuit model (Ottesen et al. 2004). Because the elastance represents cardiac function independent of loading conditions, contractile state, and heart rate (Suga et al. 1973; Suga and Sagawa 1974), its peak value was estimated from aortic pressures and ventricular volumes and the time-to-peak was estimated from heart rate (Weissler et al. 1963; Senzaki et al. 1996). Herein, initial values were derived assuming proximal aortic pressures of 120/80 mmHg, a heart rate of 60 bpm, cardiac output of 5 L/min, and an end diastolic volume of 175 mL, which represent a normal healthy adult human heart (Schlosser et al. 2005; Guyton and Hall 2006). The initial left atrial pressure was assumed to be 10 mmHg. The final heart model parameters were $P_{LA} = 11 \text{ mmHg}$, maximum elastance of 1.25 mmHg/mL, and time-to-peak elastance of 0.4 s. A Lagrange profile constraint with a penalty number of

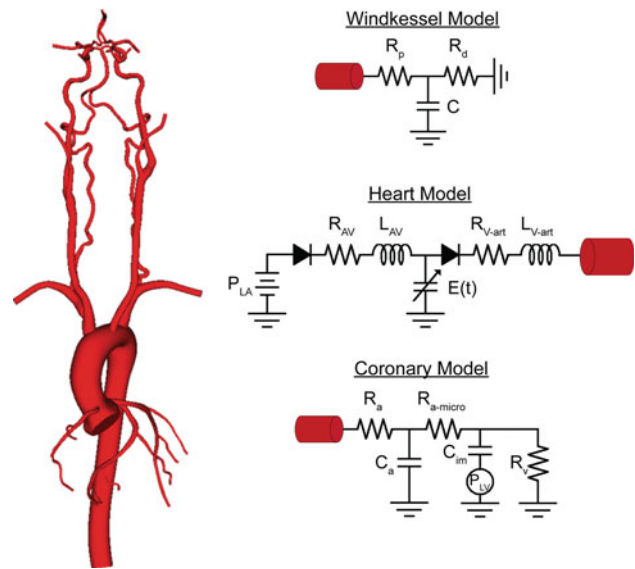


Fig. 3 Schematic of the various lumped parameter models utilized to specify boundary conditions for the 3D computational model. The Windkessel model was applied at all outlets except the coronary tree; the heart model was applied at the aortic root, and the coronary model was prescribed at all outlets of the coronary tree

10,000 was used to stabilize the solution during the systolic phase of the cardiac cycle (Kim et al. 2009a).

2.3.2 Windkessel RCR model

Hemodynamic conditions were prescribed at every outlet in the descending aorta, neck, and head vessels in terms of a proximal (larger arteries and arterioles) resistance, R_p , a proximal vessel capacitance C , and a distal (small arterioles and capillaries) resistance R_d (cf. Fig. 3). The sum of the two resistances ($R_{total} = R_p + R_d$) represented the total resistance to flow at each outlet and was estimated using the equation, $P = Q R_{total}$, where P and Q are the target mean pressure and flow, respectively. Initial values for the total resistance were computed for a MAP of 100 mmHg and mean flow prescribed based on the cross-sectional area of each outlet (Zamir et al. 1992). For simplicity, the ratio α between proximal and total resistances $\alpha = R_p / (R_p + R_d)$ was assumed to be identical for all 11 Windkessel outlets. To determine the value of the capacitance at each outlet, a value for total capacitance C_{total} was chosen and distributed through the outlets based on their cross-sectional area. Initial values for both α and C_{total} were prescribed based on previous data (Les et al. 2010). An iterative procedure was then used to modify the values of R_{total} at each outlet such that the total cerebral blood flow and external carotid blood flow were consistent with data in Scheel et al. (2000). Flow to the right and left subclavian arteries was approximately 12% of cardiac output, whereas flow through the descending aorta was

Table 1 Parameter values of the lumped parameter Windkessel and coronary models

Windkessel parameters			Coronary parameters						
Outlet	R_p	R_d	C	Outlet	R_a	$R_{a\text{-micro}}$	R_v	C_a	C_{im}
Desc Aorta	0.25	2.48	500	LAD1	176	287	91	0.28	2.41
L Subclavian	1.88	19.0	44.7	LAD2	131	214	68	0.37	3.14
R Subclavian	1.88	19.0	48.3	LAD3	126	206	66	0.38	3.26
L Ext Carotid	4.39	44.4	15.0	LAD4	75	123	39	0.61	5.19
R Ext Carotid	4.39	44.4	13.9	LCX1	48	78	25	1.07	9.17
L Ant Cerebral	11.2	113	5.23	LCX2	159	260	83	0.41	3.50
R Ant Cerebral	11.2	113	5.05	LCX3	213	348	111	0.32	2.78
L Int Carotid	3.18	32.1	11.0	LCX4	167	272	87	0.39	3.38
R Int Carotid	3.18	32.1	10.3	RCA1	166	271	86	0.59	5.07
L Post Cerebral	8.29	83.8	5.41	RCA2	231	377	120	0.44	3.74
R Post Cerebral	8.29	83.8	6.13	RCA3	258	422	134	0.39	3.38

The coronary outlets are listed from proximal to distal along the vessel indicated. The units of resistance are 10^3 dynes s/cm⁵ and the units of capacitance are 10^{-6} cm⁵/dynes

approximately 60% of cardiac output in the absence of the coarctation (Lantz et al. 1981; Scheel et al. 2000). Given that the values of α and C_{total} mostly affected the pulse pressure, these parameters were refined so that the blood pressure in the ascending aorta remained 120/80 mmHg. Finally, a Lagrange profile constraint was used at the inlet and outlet of the aorta as well as at the outlets of the right and left subclavian and external carotid arteries; the associated penalty parameter was assigned a value of 10,000. Such constraints stabilize the computed solution while affecting only the hemodynamics in a small region near the constraint (Kim et al. 2009a).

2.3.3 Coronary model

A lumped parameter model of the coronary vascular bed (Kim et al. 2010) was prescribed at the outlets of the large coronary vessels (cf. Fig. 3). In addition to the resistors and capacitance of the Windkessel model, this model included the venous circulation and incorporated effects of left ventricular pressure. The latter is critical since contraction of the heart is one of the main determinants of coronary flow. The total resistance at each outlet R_{total} was again calculated assuming a MAP of 100 mmHg and that flow through each outlet scaled with cross-sectional area, with mean coronary flow comprising approximately 4.5% of cardiac output (Zhou et al. 1999; Guyton and Hall 2006). The Windkessel portion of the lumped parameter coronary model was represented by R_a , C_a , and $R_{a\text{-micro}}$. The ratio $\alpha_c = R_a / (R_a + R_{a\text{-micro}})$ was assumed to be uniform ($\alpha_c = 0.38$) for every coronary outlet (Huis et al. 1987). The venous pressure defined the relationship between R_a , $R_{a\text{-micro}}$, and R_v and was assumed to be 15 mmHg. Two parameters, $C_{a\text{-total}}$ and $C_{im\text{-total}}$, were defined as the sum of all coronary arterial (C_a) and

intra-myocardial (C_{im}) compliances. An iterative tuning procedure was used to find values of $C_{a\text{-total}}$ and $C_{im\text{-total}}$ that yielded physiologic coronary flow waveforms. The values of C_a and C_{im} were distributed among the outlets based on their cross-sectional area. For the left coronary vessels, the left ventricular pressure found in the lumped parameter coronary model was equivalent to the pressure derived from the heart model. While the right side of the heart was not modeled directly, the boundary condition for the right coronary artery was based on a scaling of left ventricular pressure that was derived from the heart model, specifically $P_{RV} = 0.20 \cdot P_{LV}$. Hence, reasonable values of right ventricular pressure were included in the model. The final parameter values for the heart model and Windkessel models are listed in Table 1.

2.3.4 Vessel wall properties

Given current limitations in experimental data on regional variations in vascular mechanical properties and thickness, four sections of the vasculature were endowed with different but uniform wall properties, reflected by an effective constant stiffness and thickness of the wall (Fig. 4). The stiffness of the thoracic aorta was chosen to yield physiologic levels of strain over normal ranges of blood pressure (Redheuil et al. 2010) whereas moduli for coronary, neck, and cerebral vessels were based directly on data (Gow and Hadfield 1979; Hayashi et al. 1980; Nichols and O'Rourke 2005). The thickness of the vessel in each section was assumed to be 1/10 of the mean radius within that section (Nichols and O'Rourke 2005). See Table 2 for values of the requisite parameters.

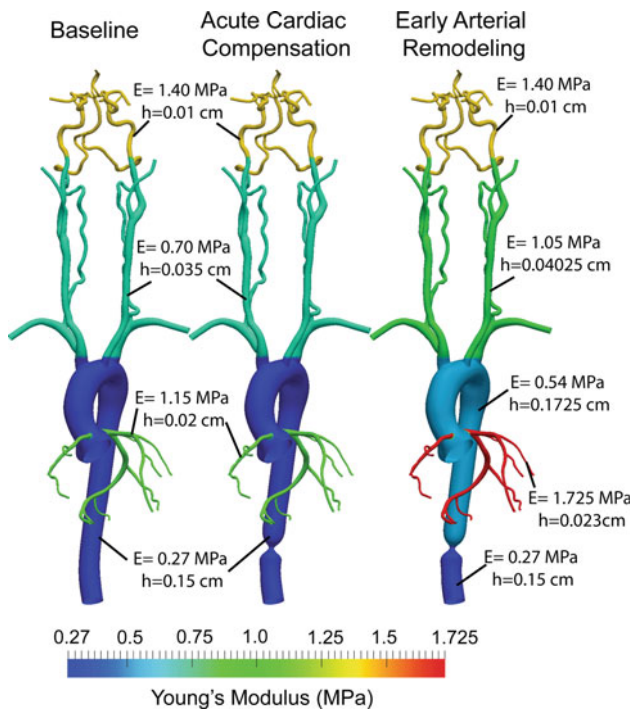


Fig. 4 Sections of the model with different wall properties. *Color scale* represents values of material stiffness adopted for each section. The acute cardiac compensation time frame refers to the introduction of coarctation and subsequent cardiac compensation, while the early arterial remodeling shows the differential stiffening observed in animal experiments in various regions of the vasculature

2.4 Acute cardiac compensation following coarctation

When first introducing the coarctation, parameters for the heart model were modified to simulate an acute cardiac compensation. This modification accounted for the increased work required of the heart to compensate for the increased afterload due to the coarctation. If the heart were not to adapt, then cardiac output would decrease due to the increased resistance in the aorta. Thus, the heart model was modified by iteratively increasing values of the maximum left ventricular elastance and left atrial pressure until cardiac output equaled that of the baseline model (Taylor and Donald 1960). We assumed that cardiac output remained unchanged since the aortic stenosis was moderate (75% diameter reduction) and that it is unlikely that either the perfusion or the metabolic

demands of the subject were altered significantly. See, for example, Giddens et al. (1976) who demonstrated that cardiac output remained nearly the same over a range of moderate, surgically induced aortic stenoses in dogs and Tropea et al. (2000) who reported that heart rate remains nearly constant in surgically induced stenosis (80–83% area reduction) in rabbits. It follows that, in order to maintain cardiac output, contractility of the heart (i.e., the elastance) must increase. In addition, changes in elastance affect filling of the heart, thus requiring an increase in left atrial pressure to maintain the same end diastolic volume. The final left atrial pressure was 14 mmHg, and the maximum elastance was 1.52 mmHg/mL.

2.5 Early arterial remodeling

Early arterial vascular remodeling (i.e., within the first 10 days or so) was simulated by modifying wall properties to reflect stiffening and thickening of the thoracic aorta proximal to the coarctation, the coronary vessels, and the neck vessels. These changes were based on findings that the pulse wave velocity can increase by as much as twofold with aging and that many adaptive processes associated with aging are similar to those associated with hypertension (Wolinsky 1972; Nichols and O'Rourke 2005). Updated values of stiffness and thickness are given in Table 2 for each section and illustrated in Fig. 4. Briefly, the stiffness of the aortic arch, coronary tree, and neck vessels was increased by 100, 50, and 50%, respectively, while the thickness was increased 15%. We assumed that the cerebral vasculature did not experience any changes in stiffness or thickness during this early period (cf. Hayenga 2010). We also did not prescribe any associated changes in vascular lumen largely because of the lack of associated experimental data and the possible competing effects of changes in distal resistances (e.g., cerebral autoregulation) and local shear-regulated vasodilatation.

The prescribed changes in vascular stiffness and thickness affected cardiac afterload, hence additional cardiac compensation was required to maintain cardiac output after arterial remodeling. The final left atrial pressure was 16 mmHg, and the maximum elastance was 1.82 mmHg/mL. All other outlet boundary conditions (arterial and coronary) remained the same for baseline, acute cardiac compensation, and early arterial remodeling.

Table 2 Vessel wall parameters for baseline, coarctation with acute cardiac compensation, and early arterial remodeling conditions

	Baseline/acute cardiac compensation		Early arterial remodeling	
	Thickness (cm)	Young's modulus (MPa)	Thickness (cm)	Young's modulus (MPa)
Aorta	0.15	0.27	0.1725	0.54
Coronary	0.02	1.15	0.023	1.725
Neck	0.035	0.7	0.04025	1.05
Cerebral	0.01	1.4	0.01	1.4

2.6 Data analysis

Simulation data were analyzed using the open-source software Paraview (Kitware, Inc. Clifton Park, NY, USA). Pressure, flow, and cyclic wall strain were analyzed at five different locations within the vasculature (see Fig. 5): the proximal descending aorta (P-Ao), left anterior descending (LAD) coronary artery, left common carotid artery (LCCA), left middle cerebral artery (LMCA), and basilar artery (BA). Mean circumferential wall strain was calculated based on changes in the cross-sectional area of the vessel over a cardiac cycle using the following Green-Lagrange type expression,

$$E_{\theta\theta} = \frac{1}{2} \left(\frac{A_t}{A_D} - 1 \right) \quad (1)$$

where A_t is the cross-sectional area at any given time t and A_D is a reference diastolic value (note: using area effectively represents radius squared as needed in the nonlinear measure of strain).

For completeness, mean circumferential wall stress was calculated using the common Laplace relation,

$$\sigma = \frac{Pa}{h} \quad (2)$$

where P is the mean transmural pressure, a the luminal radius, and h the wall thickness. The wall shear stress field on the luminal surface ($\vec{\tau}$) was calculated using a variationally consistent method (Hughes 2000). The temporal mean of the wall shear stress was evaluated as:

$$\bar{\tau}_{\text{mean}} = \frac{1}{T} \int_0^T \vec{\tau} dt \quad (3)$$

where T is the cardiac period. Nevertheless, in the figures below we focus on regional changes in cyclic pressure, flow, and wall strain, which are measurable and thus able to be compared to experimental values, when available.

3 Results

The baseline simulation provided a prototypical human aortic pressure of 120/80 mmHg, cardiac output of 5 L/min, and heart rate of 60 bpm. Associated pressure, flow, and strain waveforms also had realistic shapes (see Fig. 5). The P-Ao had the highest mean and peak strain, followed by the LCCA, BA, LAD, and LMCA. Conversely, the highest mean wall shear stress and mean circumferential stress were in the LMCA, followed by the BA, LAD, LCCA, and P-Ao. The coronary arteries exhibited realistic shapes and averages in the flow, pressure, and strain waveforms. Indeed, our results reproduced predominant diastolic flows (Kim et al. 2010), mean coronary flow values (approximately 5% of cardiac

output, Williams and Leggett 1989), realistic pressure ranges (120/80 mmHg), and average strain values (<2%, de Korte et al. 2002). In addition, equal regional blood flows were obtained in the left and right cerebral hemispheres, with mean and pulse pressure lower in the cerebral arteries than in other areas of the vasculature. These results are summarized in Fig. 5 and Table 3.

Cardiac output would have decreased from 5 to 4.46 L/min after introducing the 75% aortic coarctation if no changes were made in the lumped parameter heart model. Increasing the maximum elastance of the heart from 1.25 to 1.52 mmHg/mL maintained cardiac output at 5 L/min, but increased blood pressure in the entire model (e.g., from 120/80 to ~150/90 mmHg in the P-Ao). The pressure, flow, and strain waveforms also exhibited more oscillations in each vascular territory, possibly due to the additional reflection site at the coarctation (Fig. 6). Similar to the simulation of the baseline condition, the P-Ao had the highest mean and peak strain, followed by the LCCA, BA, LAD, and LMCA, all with values higher than those under baseline conditions. Interestingly, while the percent increase in MAP was approximately the same throughout the model, the percent increase in pulse pressure was the greatest in the P-Ao, followed by the LCCA, BA, LAD, and LMCA (Table 4). Whereas flow increased through the LAD, LCCA, LMCA, and BA, it decreased in the P-Ao, thus indicating an early redistribution of flow due to the increased resistance at the coarctation. This redistribution also explained the smaller percentage increase in wall shear stress in the P-Ao compared to the other vascular territories. Cardiac workload, as measured by the area within the pressure–volume loop of the left ventricle, increased 17% from 8,476 to 9,890 mmHg mL (see Fig. 7).

Early (e.g., one to two weeks) arterial remodeling was introduced by modifying wall properties to simulate a stiffer and thicker wall in the aorta, coronary arteries, and major neck arteries as indicated earlier (cf. Table 2). If the heart model was not modified, these changes in arterial properties would have decreased cardiac output from 5 to 4.59 L/min. Additional cardiac compensation was thus introduced (e.g., increased maximum elastance to 1.82 mmHg/mL) to maintain cardiac output at 5 L/min. This change resulted in yet another increase in blood pressure throughout the model, with aortic blood pressure reaching ~180/80 mmHg. Additional oscillations were seen in the pressure, flow, and strain waveforms compared with those found in the acute cardiac compensation stage (Fig. 6). The P-Ao again had the highest mean and peak strain, followed by the BA, LCCA, LMCA, and LAD. In this case, wall strain returned to near baseline levels in the P-Ao, whereas strains in the LCCA and LAD were approximately the same as for acute cardiac compensation despite the stiffening and thickening experienced by these arteries. Lastly, strains in the LMCA and BA were higher than those seen with acute cardiac compensation due

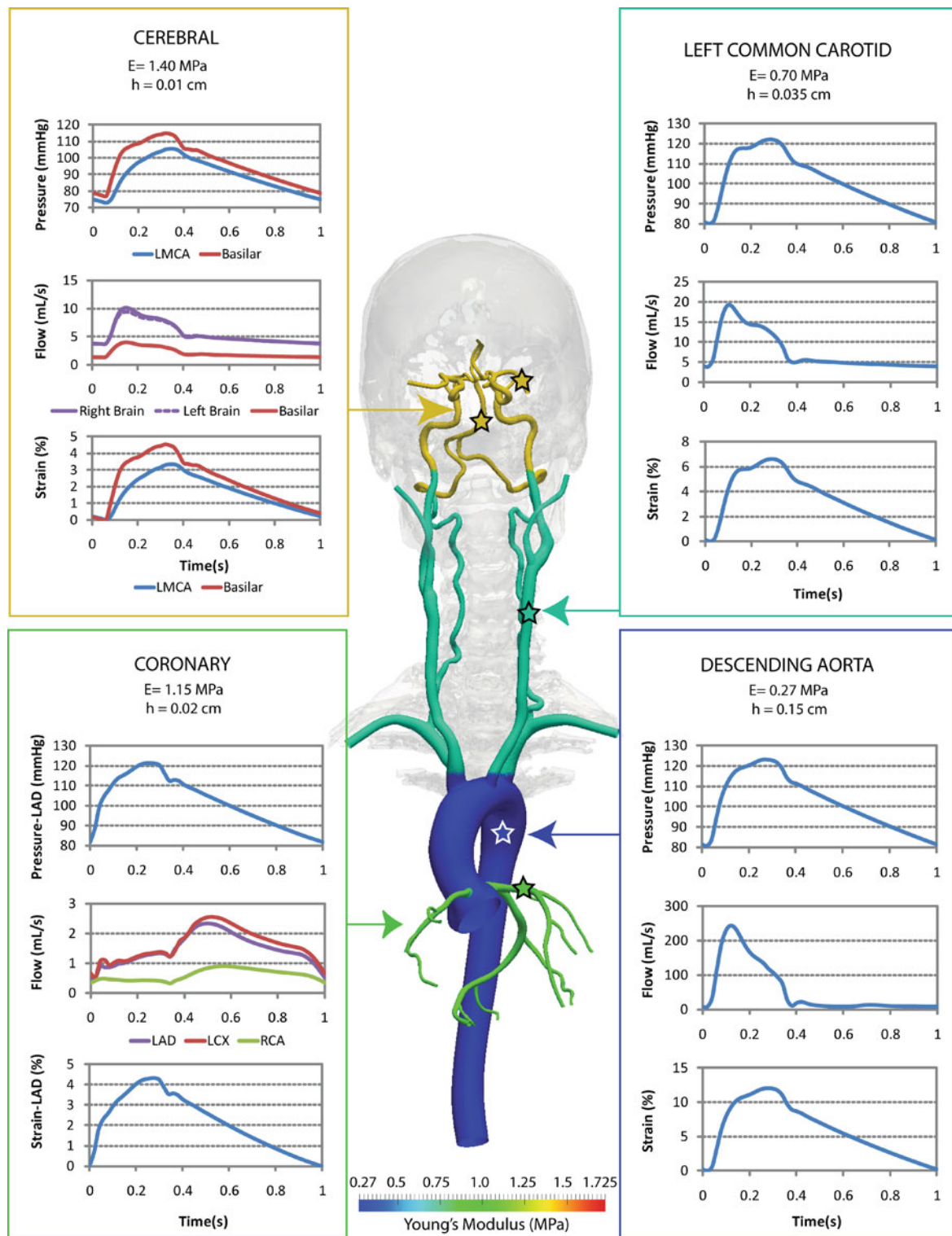


Fig. 5 Results for the baseline simulation. Pressure, flow, and wall strain are shown in each of the four primary arteries of interest. The location of the stars corresponds to the descending thoracic aorta, left anterior descending (LAD) coronary artery, left internal carotid artery, basilar artery (BA), and left middle cerebral artery (LMCA). The diameter of each of these vessels is: descending thoracic aorta=2.1 cm, LAD coronary artery=0.5 cm, left internal carotid artery=0.7 cm,

basilar artery=0.3 cm, and left middle cerebral artery=0.3 cm. For the coronary vasculature, pressure, and strain are calculated in the LAD, whereas the flow corresponds to the sum over the large coronary vessels (LAD; left circumflex, LCX; and right coronary artery, RCA). For the cerebral vasculature, pressure and strain are calculated in the LMCA and BA, and flow is calculated as the total flow in the right and left cerebral hemispheres as well as in the BA

Table 3 Summary of results for all three simulations: baseline, acute cardiac compensation, and early arterial remodeling

	Baseline					Acute cardiac compensation					Early arterial remodeling				
	Aorta	LAD	LCCA	LMCA	Basilar	Aorta	LAD	LCCA	LMCA	Basilar	Aorta	LAD	LCCA	LMCA	Basilar
P_{mean} (mmHg)	102	102	101	89	96	121	121	120	105	114	124	124	123	106	116
PP (mmHg)	42	40	42	33	38	70	60	65	47	58	101	97	97	74	88
Q_{mean} (mL/s)	54.5	1.2	7.5	3.4	2.1	47.7	1.5	8.9	4.0	2.5	45.6	1.5	9.0	4.0	2.6
$E_{\theta\theta}^{\text{mean}}$ (%)	5.9	2.2	3.2	1.7	2.3	8.9	3.2	4.8	2.4	3.6	5.8	2.9	4.4	3.7	5.3
$E_{\theta\theta}^{\text{peak}}$ (%)	12.0	4.3	6.6	3.4	4.5	20.6	6.6	10.3	4.9	7.1	12.6	6.2	9.5	8.0	10.9
$\bar{\tau}_{\text{mean}}$ (Pa)	0.98	1.12	1.11	9.57	3.59	1.01	1.40	1.41	11.82	4.56	0.78	1.43	1.58	12.58	4.91
σ_{mean} (kPa)	94	153	141	164	204	112	182	167	193	242	100	162	149	195	247

P mean arterial pressure, PP pulse pressure, Q flow, $E_{\theta\theta}$ cyclic strain, $\bar{\tau}$ wall shear stress, σ circumferential wall stress

to the higher mean and pulse pressures, but no changes in wall properties. The mean values of circumferential stress were between those for baseline and acute cardiac compensation for the P-Ao, LCCA, and LAD, but higher in the basilar artery and LMCA. When comparing acute cardiac compensation and early arterial remodeling, the percent increase in mean pressure was nearly identical throughout the entire model but the percent increase in pulse pressure differed regionally, being largest in the LAD, then LMCA, BA, LCCA, and P-Ao (Table 4). This finding emphasizes that possible differential changes in pulse, not mean, pressure throughout the vasculature might be responsible for different time courses of arterial remodeling. Flow through the LAD, LCCA, LMCA, and BA increased, whereas flow through the P-Ao decreased further, indicating an additional redistribution of flow. Cardiac workload increased 12% from 9,890 to 11,059 mmHg mL (see Fig. 7). Pressure wave speeds were estimated by determining the length between the aortic inlet and the LMCA and the time between the foot of the aortic and LMCA pressure contour. Due primarily to the increased structural stiffness throughout the aorta and neck vessels, wave speed increased relative to baseline values (Fig. 8).

4 Discussion

The composition, microstructure, and material properties of blood vessels differ markedly with position along the vascular tree to meet local demands—that is, normal structure clearly follows normal function. Consequently, it has proven convenient to classify vessels broadly as elastic arteries, muscular arteries, arterioles, capillaries, venules, or veins. Findings over the past few decades have revealed that vessels within these different classifications respond differently to altered biomechanical stimuli. For example, whereas all arteries and arterioles tend to thicken in response to hypertension, the elastic arteries, muscular arteries, and arterioles tend to do so while increasing, maintaining, and decreasing their caliber, respectively (Humphrey 2002). Precise reasons

for these different responses remain elusive, but likely result in part from the different distributions of intramural constituents, including the different embryonic lineages, phenotypes, and percentages of smooth muscle cells.

More recently, it has become apparent that differential remodeling responses can even occur within vessels of the same general classification and within close proximity to one another. For example, the ascending aorta (an elastic artery) appears to be the first central artery (i.e., of the rest of the aorta and carotids) to manifest aging-related changes in structure that affect overall mechanical properties (Redheuil et al. 2010). Among the many effects of aging on arteries (including increased endothelial dysfunction and advanced glycation endproducts; Lakatta et al. 2009; Safar 2010), it appears that a fatigue-type damage to elastic fibers is particularly important (Arribas et al. 2006; O'Rourke and Hashimoto 2007). Indeed, it may well be that the increased susceptibility of the ascending aorta to an aging-related loss of elastic fiber integrity may explain in part the increased susceptibility of the same region to dilatation and dissection in Marfan syndrome (Pearson et al. 2008), which results from a genetic mutation in the fibrillin-1 gene (FBN1); fibrillin-1 appears to help stabilize elastic fibers, hence mutations in FBN1 also result in decreased elastic fiber integrity.

Understanding better the spatio-temporal progression of vascular changes in both adaptive and maladaptive G&R could impact clinical care significantly. For example, being able to identify early indicators of vascular disease or subsequent risk could allow earlier interventions, before the subsequent disease presents symptomatically as heart attack, stroke, or other life threatening condition. A long-term goal of this work is to build a new class of computational models that aid in understanding local and systemic effects of spatially and temporally progressive changes in large portions of the vascular tree and attendant changes in the hemodynamics, which in turn serve as strong mechanobiological stimuli for subsequent vascular growth and remodeling. Toward that end, here we presented a zeroth order model wherein progressive changes in large segments of the vasculature (e.g.,

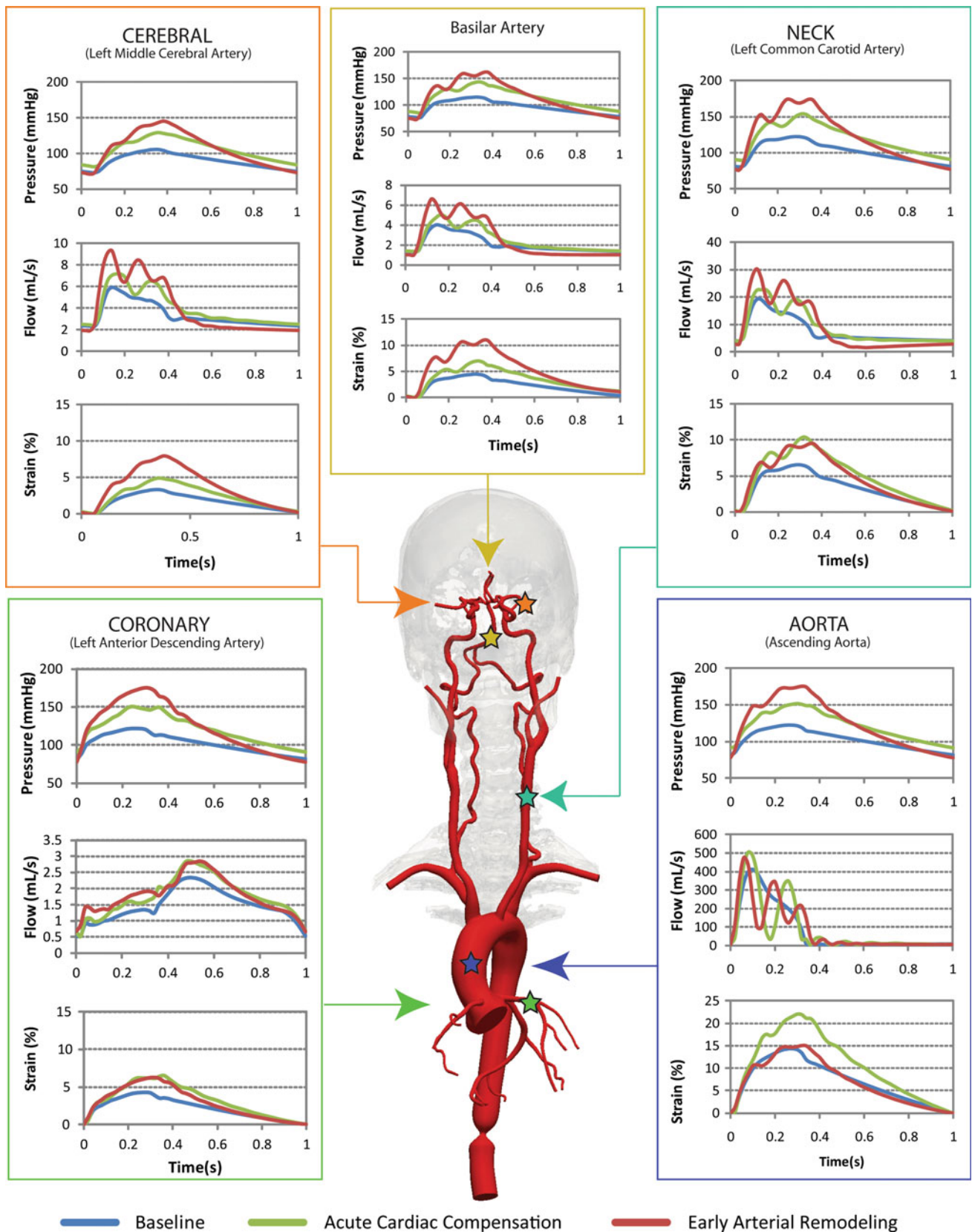


Fig. 6 Results comparing pressure, flow, and wall strain in baseline, acute cardiac compensation, and early arterial remodeling conditions. The location of each measurement is denoted by the color-coded stars

Table 4 Simulation-based results expressed as percent changes between baseline and acute cardiac compensation, baseline and early arterial remodeling, and acute cardiac compensation and early arterial remodeling

	Baseline versus acute (%)					Baseline versus early remodeling (%)					Acute versus early remodeling (%)				
	Aorta	LAD	LCCA	LMCA	Basilar	Aorta	LAD	LCCA	LMCA	Basilar	Aorta	LAD	LCCA	LMCA	Basilar
ΔP_{mean}	19	19	19	18	19	22	22	22	19	21	2	2	3	1	2
ΔPP	67	50	55	42	53	140	143	131	124	132	44	62	49	57	52
ΔQ_{mean}	-12	26	19	16	19	-16	28	20	19	24	-4	2	1	2	4
$\Delta E_{\theta\theta}^{\text{mean}}$	51	45	50	41	52	-2	32	38	118	130	-35	-9	-8	54	51
$\Delta E_{\theta\theta}^{\text{peak}}$	72	53	56	44	58	5	44	44	135	142	-39	-6	-8	63	54
$\Delta \tau_{\text{mean}}$	3	25	27	24	27	-20	28	42	31	37	-23	2	12	6	8
$\Delta \sigma_{\text{mean}}$	19	19	18	18	19	6	6	6	19	21	-11	-11	-11	1	2

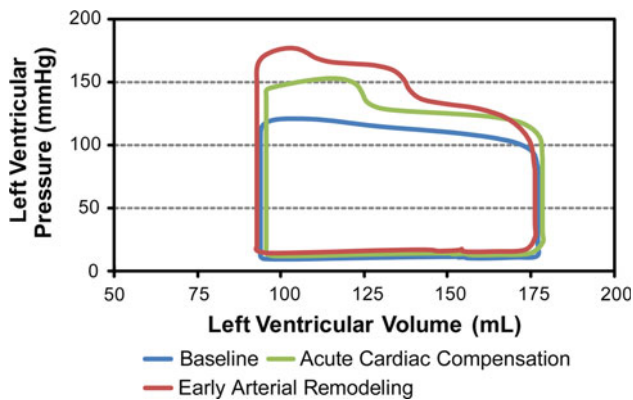


Fig. 7 Pressure–volume loops reflecting the workload of the left ventricle during baseline conditions, acute cardiac compensation, and early arterial wall remodeling. The cardiac workload was 8,476, 9,890, and 11,059 mmHg mL for the baseline, acute cardiac compensation, and early arterial remodeling simulations, respectively

thoracic aorta versus major neck arteries versus major coronary arteries) were introduced based on limited observations in the literature to study possible consequences on the associated hemodynamics. Specifically, motivated by animal models of increased blood pressure / pulse pressure (Xu et al. 2000; Hu et al. 2008; Eberth et al. 2009; Hayenga 2010), we studied the potential short-term (first week) effects of the abrupt creation of a 75% coarctation in the human descending thoracic aorta.

4.1 Baseline state

The baseline simulation revealed hemodynamic characteristics for normal, healthy individuals. Use of appropriate wall properties and inlet / outlet boundary conditions led to reasonable values of pressure, flow, and strain in a large vascular model comprising vessels in the thorax, neck, and head. Normal aortic pressure is widely considered as 120/80 mmHg, which was found in this simulation as well. The pressure contour was also physiologic, with the reflected pressure wave

occurring in mid-systole, similar to the pressure pulse seen in middle-aged individuals (Nichols and O'Rourke 2005). The pressure contours in the LAD, LCCA, and BA did not differ appreciably from that in the aorta, but the contour in the LMCA demonstrated a reduced pulse pressure consistent with measurements in animals (Himwich and Spurgeon 1968). The simulated flows were also similar to those measured experimentally, including phase-contrast MRI and Doppler ultrasound data for the aorta and cerebral vessels (Reymond et al. 2009) and Doppler ultrasound data for coronary vessels (Hozumi et al. 1998). While we used a simplified Green-Lagrange equation to estimate wall strain relative to diastole (which includes a factor of 0.5), many studies measure strain either as a relative change in diameter or luminal area, for example $(D_{\text{max}} - D_{\text{min}})/D_{\text{min}}$ or $(A_{\text{max}} - A_{\text{min}})/A_{\text{min}}$. When recalculated in the latter way, relative changes in luminal area were found to be $\sim 20\%$ in the aorta, which corresponds well with values in literature for middle-aged individuals (cf. Redheuil et al. 2010). The relative change in luminal area was $\sim 13\%$ in the carotid, which also corresponded well with reported values (cf. Nagai et al. 1999). Strain is difficult to measure in coronary and cerebral vessels, hence the computational results provide new estimates for these regions.

4.2 Acute cardiac compensation state

Introducing a coarctation in the distal descending aorta altered mean and pulse pressures in the proximal vessels as well as the after-load felt by the heart. We estimated that an abrupt 75% coarctation increased the workload of the heart $\sim 17\%$. While all vascular regions had nearly equal increases in mean arterial pressures, the descending aorta proximal to the coarctation (P-Ao) experienced the largest increase in pulse pressure while the left middle cerebral artery experienced the smallest increase. Because pulse pressure has been suggested to be a more important modulator of wall adaptation than mean pressure (Eberth et al. 2010), the

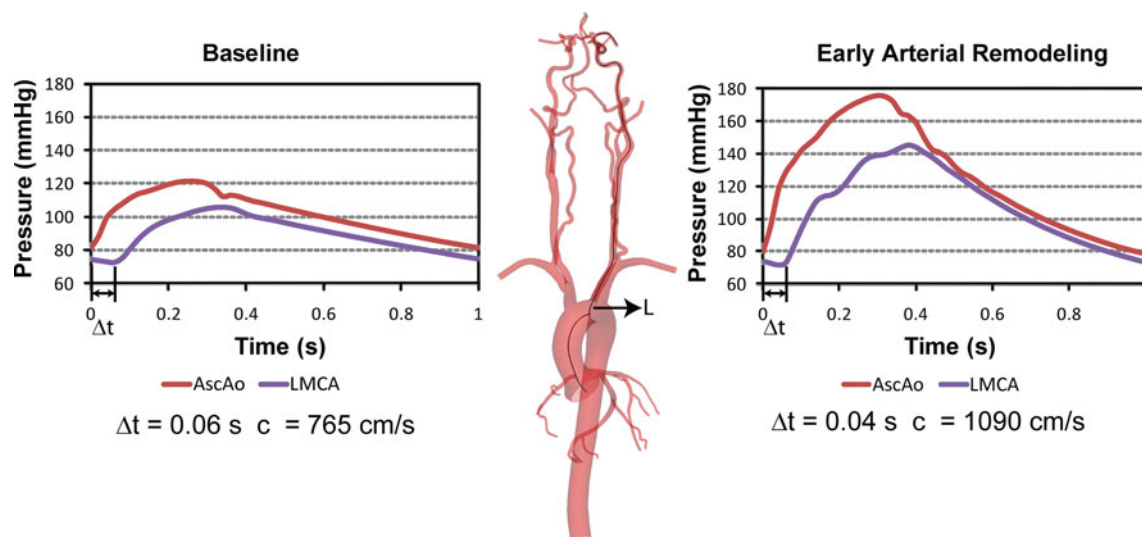


Fig. 8 Pressure contours during baseline conditions and early arterial remodeling. Increased wave speed is apparent in the vascular adaptation case. L denotes the path length from the aortic root to the LMCA,

Δt denotes the time between the feet of the aortic and LMCA pressure contours, and c denotes the wave speed

smaller change in pulse pressure in the cerebral arteries may explain the lack of marked early remodeling in those arteries in response to hypertension (Hayenga 2010). Note, too, that when moving away from the coarctation, less change was seen in the pulse pressure, possibly suggesting that a “wave of remodeling” could result, with regions closest to the coarctation remodeling first. These increases in pulse pressure directly affect cyclic wall stress and strain, which may correlate with mechanical stimuli sensed by intramural cells. By including multiple vascular territories within a single model, effects of wave reflection were seen. Given that the coarctation represented an additional site for wave reflection, it was not surprising that increased oscillations were seen in the pressure and flow contours. The oscillations in pressure appeared to dissipate in the coronary and cerebral vessels, however, which may suggest a dampening of the reflected waves as they travel farther from the site of reflection.

4.3 Early arterial remodeling

Arterial remodeling was introduced in the aorta, coronary, and neck vessels in a manner consistent with the hypothesis of a wave of remodeling. In the short term, the thoracic aorta should experience the greatest changes in wall properties, followed by the coronary and neck vessels, and (eventually) the intracranial vessels. Increasing the stiffness in these regions led to an increase in the after-load felt by the heart comparable to that associated with the introduction of coarctation. This finding emphasizes that increased arterial stiffness can have a significant impact on the cardiovascular system. Arterial remodeling appears to attempt to maintain circumferential wall stress near normal values by remodeling the wall and

changing vessel thickness in response to changes in mean pressure. Calculated values of circumferential stress did not return to its baseline level at any location, which may be expected for a short-term adaptation. Thickness would be expected to increase further over the long term (cf. Eberth et al. 2010).

Interestingly, three different strain responses were noted following the prescribed early remodeling: strain returned to baseline levels in the aorta, they were equivalent to the case of acute cardiac compensation in the coronary and neck vessels, and they were higher than those for cardiac compensation in the cerebral vessels. These three responses corresponded with the three different prescribed vascular wall adaptations—stiffness and thickness were prescribed to increase, respectively, 100 and 15% in the aorta but only 50 and 15% in the coronary and neck vessels and not at all in the cerebral vessels. Such changes are difficult to predict without a FSI model since a stiffer wall would be expected to reduce wall strain, but it also alters pulse wave propagation and thus pulse pressure, which can increase strain. In our simulations, larger increases in stiffness led to lower strains nonetheless. Increased oscillations were also seen in the pressure and flow contours as expected since stiffer arteries propagate wave reflections faster. Indeed, wave speed was found to be significantly higher with the incorporation of arterial remodeling.

Notwithstanding new insights gained from the present model, there is a need to couple directly an arterial growth and remodeling code (cf. Valentín et al. 2009) with a fluid–solid interaction code (e.g., SimVascular) to create a true fluid–solid–growth model (FSG) (cf. Figueroa et al. 2009). Toward this end, there is need for better data on the differential composition, material properties, vasoactivity, and remodeling

responses of the different arteries that define each segment of the vasculature of interest. For example, only recently did [Haskett et al. \(2010\)](#) present the first detailed comparison of the structure and passive biaxial mechanical properties from the ascending aorta to the arch, descending thoracic, and suprarenal and infrarenal abdominal aorta in human subjects as a function of age. Similarly, only recently did [Wagner and Humphrey \(2011\)](#) present the first direct comparison of the biaxial active and passive mechanical properties of related extracranial (carotid) and intracranial (basilar) arteries, albeit for rabbits, not humans, and not as a function of age. Much more data are needed, particularly to include changes in endothelial function/smooth muscle contractility because of the important coupling between vasoactivity and matrix remodeling ([Dajnowiec and Langille 2007](#); [Valentín et al. 2009](#)). We submit, however, that the present work shows that once such data are available, computational methods are now sufficient to allow detailed studies of large portions of patient-specific vasculatures to provide increasing insight into changes in both the hemodynamics and wall mechanics.

4.4 Limitations

Prescribing boundary conditions is both difficult and critical in any computational model. Although considerable effort was devoted to identifying physiologically realistic boundary conditions herein, the associated results are not yet expected to be fully physiologic. As with any model, more experimental data are needed to improve the simulations. Nevertheless, the present study reminds us that even if interested in a local effect, systemic effects must be considered. For example, when the coarctation was introduced, we only changed the heart model and certain proximal arterial properties, which neglected possible vascular adaptation distal to the coarctation. Of particular concern are changes resulting from altered renal perfusion. In addition, changes in the coronary and cerebral microcirculations might be expected. Such adaptations were neglected primarily because of a lack of experimental data to prescribe changes in distal vascular resistances following the introduction of aortic coarctation. As a result, the computed values of blood pressure may be higher than would be found in a model that incorporates evolving distal vascular resistances. We also only considered short-term adaptations since longer-term adaptations could include the formation of collateral vessels around the coarctation (cf. [Aguirre-Sanceledonio et al. 2003](#)) that would be difficult to simulate without data. Furthermore, the time scales associated with the production of a coarctation will differ in human disease processes and animal models. Although the former is our ultimate goal, our present results were motivated by the latter ([Hayenga 2010](#)). As simulations continue to move toward full fluid–solid–growth simulations, prescribing uniform wall properties within different segments of the arterial

tree will need to give way to smoothly varying properties, which will necessitate more complete experimental data and computational advances such as that suggested by [Bazilevs et al. \(2009a,b\)](#). Future work will also incorporate closed-loop lumped parameter models of the circulation that include both left and right sides of the heart ([Kim et al. 2010](#); [Baretta et al. 2011](#); [Balossino et al. 2009](#)) to better account for global circulatory changes in response to local changes in geometry and material properties. Our fluid–solid interaction model did not incorporate large motions and deformations that might be expected in the coronary vessels since they are embedded in the beating myocardium. Numerous studies have quantified large myocardial strains (>20%, [Osman et al. 2000](#); [Prummer et al. 2007](#)), coronary artery motion (>10 mm, [Zhang et al. 2009](#); [Hoffman et al. 1998](#)), and stretching, bending, and twisting ([Choi et al. 2008](#)). It should be remembered, however, that left coronary flow occurs primarily during diastole, hence one need not model the full range of strains with respect to flow; modeling distal coronary resistances is probably most important in restricting flow to the appropriate period during diastole. Finally, from a growth and remodeling perspective, the impact that cyclic alterations in these strains have on the mechanobiology of the coronary arteries is also currently not understood and is clearly unique relative to most other arteries. Nevertheless, the present framework provides the first 3-D model capable of incorporating such data when available, thus allowing us to explore potential coupled consequences of altered hemodynamics and wall remodeling in patient-specific vasculatures.

Acknowledgments This work was supported, in part, by NIH grant HL-105297 and the Benchmark Fellowship in Congenital Cardiovascular Engineering in association with the Vera Moulton Wall Center at Stanford. The authors acknowledge Dr. Charles A. Taylor for his insightful discussions and for generously providing computer resources. We also wish to acknowledge the use of the linear algebra package *AcuSolve*TM (<http://www.acusim.com>) and the mesh generator *MeshSim*TM (<http://www.simmetrix.com>).

References

- Aguirre-Sanceledonio M, Fossum TW, Miller MW, Humphrey JD, Berridge BR, Herraes P (2003) Collateral circulation in experimental coarctation of the aorta in minipigs: a possible association with hypertrophied vasa vasorum. *J Comp Pathol* 128:165–171
- Arribas SM, Hinek A, González MC (2006) Elastic fibres and vascular structure in hypertension. *Pharmacol Ther* 111(3):771–791
- Balossino R, Pennati G, Migliavacca F, Formaggia L, Veneziani A, Tuveri M, Dubini G (2009) Computational models to predict stenosis growth in carotid arteries: which is the role of boundary conditions?. *Comput Methods Biomech Biomed Eng* 12(1): 113–123
- Baretta A, Corsini C, Yang W, Vignon-Clementel IE, Marsden AL, Feinstein JA, Hsia TY, Dubini G, Migliavacca F, Pennati G (2011) Virtual surgeries in patients with congenital heart disease: a multi-scale modelling test case. *Philos Trans R Soc A* 369: 4316–4330

- Bazilevs Y, Hsu MC, Benson DJ, Sankaran S, Marsden AL (2009) Computational fluid-structure interaction: methods and application to a total cavopulmonary connection. *Comput Mech* 45:77–89
- Bazilevs Y, Gohean JR, Hughes TJR, Moser RD, Zhang Y (2009) Patient-specific isogeometric fluid-structure interaction analysis of thoracic aortic blood flow due to implantation of the Jarvik 2000 left ventricular assist device. *Comput Methods Appl Mech Eng* 198(45–46):3534–3550
- Chien S, Li S, Shyy YJ (1998) Effects of mechanical forces on signal transduction and gene expression in endothelial cells. *Hypertension* 31(1 Pt 2):162–169
- Choi G, Cheng CP, Wilson NM, Taylor CA (2008) Methods for quantifying three-dimensional deformation of arteries due to pulsatile and non-pulsatile forces: implications for the design of stents and stent grafts. *Ann Biomed Eng* 37(1):14–33
- Coogan JS, Chan FP, Taylor CA, Feinstein JA (2011) Computational fluid dynamic simulations of aortic coarctation comparing the effects of surgical- and stent-based treatments on aortic compliance and ventricular workload. *Catheter Cardiovasc Interv* 77(5):680–691
- Dajnowiec D, Langille BL (2007) Arterial adaptations to chronic changes in haemodynamic function: coupling vasomotor tone to structural remodelling. *Clin Sci (Lond)* 113(1):15–23
- Dart AM, Kingwell BA (2001) Pulse pressure—a review of mechanisms and clinical relevance. *J Am Coll Cardiol* 37(4):975–984
- de Korte CL, Carlier SG, Mastik F, Doyley MM, van der Steen AFW, Serruys PW, Bom N (2002) Morphological and mechanical information of coronary arteries obtained with intravascular elastography. *Eur Heart J* 23:405–413
- Eberth JF, Gresham VC, Reddy AK, Popovic N, Wilson E, Humphrey JD (2009) Importance of pulsatility in hypertensive carotid artery growth and remodeling. *J Hypertens* 27(10):2010–2021
- Eberth JF, Popovic N, Gresham VC, Wilson E, Humphrey JD (2010) Time course of carotid artery growth and remodeling in response to altered pulsatility. *Am J Physiol Heart Circ Physiol* 299(6):H1875–H1883
- Figueroa C, Baek S, Taylor C, Humphrey J (2009) A computational framework for coupled solid-fluid-growth mechanics in cardiovascular simulations. *Comput Methods Appl Mech Eng* 198:3583–3602
- Figueroa CA, Vignon-Clementel IE, Jansen KC, Hughes TJ, Taylor CA (2006) A coupled momentum method for modeling blood flow in three-dimensional deformable arteries. *Comput Methods Appl Mech Eng* 195:5685–5706
- Gibbons GH, Dzau VJ (1994) The emerging concept of vascular remodeling. *N Engl J Med* 330(20):1431–1438
- Giddens DP, Mabon RF, Cassanova RA (1976) Measurements of disordered flows distal to subtotal vascular stenosis in the thoracic aortas of dogs. *Circ Res* 39:112–119
- Gow BS, Hadfield CD (1979) The elasticity of canine and human coronary arteries with reference to postmortem changes. *Circ Res* 45(5):588–594
- Guyton AC, Hall JE (2006) *Textbook of medical physiology*. Saunders, Philadelphia
- Haskett D, Johnson G, Zhou A, Utzinger U, Geest JV (2010) Microstructural and biomechanical alterations of the human aorta as a function of age and location. *Biomech Model Mechanobiol* 9:725–736
- Hayashi K, Handa H, Nagasawa S, Okumura A, Moritake K (1980) Stiffness and elastic behavior of human intracranial and extracranial arteries. *J Biomech* 13(2):175–184
- Hayenga HN (2010) *Mechanics of atherosclerosis, hypertension-induced growth, and arterial remodeling*. Ph.D. dissertation, Texas A&M University, TX, USA
- Himwich WA, Spurgeon HA (1968) Pulse pressure contours in cerebral arteries. *Acta Neurol Scand* 44(1):43–56
- Hozumi T, Yoshida K, Akasaka T, Asami Y, Ogata Y, Takagi T, Kaji S, Kawamoto T, Ueda Y, Morioka S (1998) Noninvasive assessment of coronary flow velocity and coronary flow velocity reserve in the left anterior descending coronary artery by doppler echocardiography: comparison with invasive technique. *J Am Coll Cardiol* 32(5):1251–1259
- Hoffman MBM, Wickline SA, Lorenz CH (1998) Quantification of in-plane motion of the coronary arteries during the cardiac cycle: implications for acquisition window duration for MR flow quantification. *JMRI* 8(3):568–576
- Hu J-J, Ambrus A, Fossum TW, Miller MW, Humphrey JD, Wilson E (2008) Time courses of growth and remodeling of porcine aortic media during hypertension: a quantitative immunohistochemical examination. *J Histochem Cytochem* 56(4):359–370
- Hughes TJR (2000) *The finite element method. Linear static and dynamic finite element analysis*. Dover, New York
- Huis GAV, Sipkema P, Westerhof N (1987) Coronary input impedance during cardiac cycle as determined by impulse response method. *Am J Physiol* 253(2 Pt 2):H317–H324
- Humphrey JD (2002) *Cardiovascular solid mechanics. Cells, tissues, and organs*. Springer, New York
- Humphrey JD (2008) Mechanisms of arterial remodeling in hypertension: coupled roles of wall shear and intramural stress. *Hypertension* 52(2):195–200
- Humphrey JD, Taylor CA (2008) Intracranial and abdominal aortic aneurysms: similarities, differences, and need for a new class of computational models. *Annu Rev Biomed Eng* 10:221–246
- Kim HJ, Figueroa CA, Hughes TJ, Jansen KE, Taylor CA (2009) Augmented lagrangian method for constraining the shape of velocity profiles at outlet boundaries for three-dimensional finite element simulations of blood flow. *Comput Methods Appl Mech Eng* 198:3551–3566
- Kim HJ, Vignon-Clementel IE, Coogan JS, Figueroa CA, Jansen KE, Taylor CA (2010) Patient-specific modeling of blood flow and pressure in human coronary arteries. *Ann Biomed Eng* 38(10):3195–3209
- Kim HJ, Vignon-Clementel IE, Figueroa CA, LaDisa JF, Jansen KE, Feinstein JA, Taylor CA (2009) On coupling a lumped parameter heart model and a three-dimensional finite element aorta model. *Ann Biomed Eng* 37(11):2153–2169
- LaDisa JF, Taylor CA, Feinstein JA (2010) Aortic coarctation: recent developments in experimental and computational methods to assess treatments for this simple condition. *Prog Pediatr Cardiol* 30(1):45–49
- LaDisa JF, Figueroa CA, Vignon-Clementel IE, Kim HJ, Xiao N, Ellwein LM, Chan FP, Feinstein JA, Taylor CA (2011) Computational simulations for aortic coarctation: representative results from a sampling of patients. *J Biomech Eng* 133(9):0910091
- LaDisa JF, Dholakia RJ, Figueroa CA, Vignon-Clementel IE, Chan FP, Samyn MM, Cava JR, Taylor CA, Feinstein JA (2011) Computational simulations demonstrate altered wall shear stress in aortic coarctation patients previously treated by resection with end-to-end anastomosis. *Congenit Heart Dis* 6:432–443
- Lakatta EG, Wang M, Najjar SS (2009) Arterial aging and subclinical arterial disease are fundamentally intertwined at macroscopic and molecular levels. *Med Clin N Am* 93(3):583–604. (Table of Contents)
- Langille BL (1996) Arterial remodeling: relation to hemodynamics. *Can J Physiol Pharmacol* 74(7):834–841
- Lantz BM, Foerster JM, Link DP, Holcroft JW (1981) Regional distribution of cardiac output: normal values in man determined by video dilution technique. *Am J Roentgenol* 137(5):903–907
- Laurent S, Boutouyrie P, Lacolley P (2005) Structural and genetic bases of arterial stiffness. *Hypertension* 45(6):1050–1055

- Les AS, Shadden SC, Figueroa CA, Park JM, Tedesco MM, Herfkens RJ, Dalman RL, Taylor CA (2010) Quantification of hemodynamics in abdominal aortic aneurysms during rest and exercise using magnetic resonance imaging and computational fluid dynamics. *Ann Biomed Eng* 38(4):1288–1313
- Matsumoto T, Hayashi K (1994) Mechanical and dimensional adaptation of rat aorta to hypertension. *J Biomech Eng* 116(3):278–283
- Moghadam ME, Bazilevs Y, Hsia TY, Vignon-Clementel IE, Marsden AL (2011) A comparison of outlet boundary treatments for prevention of backflow divergence with relevance to blood flow simulations. *Comput Mech* 48(3):277–291
- Moireau P, Xiao N, Astorino M, Figueroa CA, Chapelle D, Taylor CA, Gerbeau J-F (2012) External tissue support and fluid-structure simulation in blood flows. *Biomech Model Mechanobiol* 11(1):1–18
- Nagai Y, Fleg JL, Kemper MK, Rywik TM, Earley CJ, Metter EJ (1999) Carotid arterial stiffness as a surrogate for aortic stiffness: relationship between carotid artery pressure-strain elastic modulus and aortic pulse wave velocity. *Ultrasound Med Biol* 25(2):181–188
- Nichols WW, O'Rourke MF (2005) McDonald's blood flow in arteries: theoretical, experimental, and clinical principles. Hodder Arnold, London
- O'Rourke MF, Hashimoto J (2007) Mechanical factors in arterial aging: a clinical perspective. *J Am Coll Cardiol* 50(1):1–13
- Osman NF, McVeigh ER, Prince JL (2000) Imaging heart motion using harmonic phase MRI. *IEEE Trans Med Imag* 19(3):186–202
- Ottesen J, Olufsen M, Larsen J (2004) Applied mathematical models in human physiology. SIAM, Philadelphia
- Pearson GD, Devereux R, Loeys B, Maslen C, Milewicz D, Pyeritz R, Ramirez F, Rifkin D, Sakai L, Svensson L, Wessels A, Eyk JV, Dietz HC, National Heart L, Institute B, Group NMF (2008) Report of the national heart, lung, and blood institute and national marfan foundation working group on research in marfan syndrome and related disorders. *Circulation* 118(7):785–791
- Prummer M, Fahrig R, Wigstrom L, Boese J, Lauritsch G, Strobel N, Hornegger J (2007) Cardiac C-arm CT: 4D non-model based heart motion estimation and its application. *Proc SPIE* 6510:651015-1-12
- Redheuil A, Yu W-C, Wu CO, Mousseaux E, de Cesare A, Yan R, Kachenoura N, Bluemke D, Lima JAC (2010) Reduced ascending aortic strain and distensibility: earliest manifestations of vascular aging in humans. *Hypertension* 55(2):319–326
- Reymond P, Merenda F, Perren F, Rüfenacht D, Stergiopoulos N (2009) Validation of a one-dimensional model of the systemic arterial tree. *Am J Physiol Heart Circ Physiol* 297(1):H208–H222
- Safar ME (2000) Pulse pressure, arterial stiffness, and cardiovascular risk. *Curr Opin Cardiol* 15(4):258–263
- Safar ME (2010) Arterial aging—hemodynamic changes and therapeutic options. *Nat Rev Cardiol* 7(8):442–449
- Safar ME, Boudier HS (2005) Vascular development, pulse pressure, and the mechanisms of hypertension. *Hypertension* 46(1):205–209
- Sahni O, Muller J, Jansen KE, Shephard MS, Taylor CA (2006) Efficient anisotropic adaptive discretization of the cardiovascular system. *Comput Methods Appl Mech Eng* 195:5634–5655
- Scheel P, Ruge C, Petrucci UR, Schöning M (2000) Color duplex measurement of cerebral blood flow volume in healthy adults. *Stroke* 31(1):147–150
- Schlösser T, Pagonidis K, Herborn CU, Hunold P, Waltering K-U, Lauenstein TC, Barkhausen J (2005) Assessment of left ventricular parameters using 16-mdct and new software for endocardial and epicardial border delineation. *Am J Roentgenol* 184(3):765–773
- Senzaki H, Chen CH, Kass DA (1996) Single-beat estimation of end-systolic pressure-volume relation in humans. a new method with the potential for noninvasive application. *Circulation* 94(10):2497–2506
- Simvascular: Cardiovascular Modeling and Simulation Application (2007) <https://simtk.org/home/simvascular>
- Suga H, Sagawa K (1974) Instantaneous pressure–volume relationships and their ratio in the excised, supported canine left ventricle. *Circ Res* 35(1):117–126
- Suga H, Sagawa K, Shoukas AA (1973) Load independence of the instantaneous pressure–volume ratio of the canine left ventricle and effects of epinephrine and heart rate on the ratio. *Circ Res* 32(3):314–322
- Taylor CA, Figueroa CA (2009) Patient-specific modeling of cardiovascular mechanics. *Annu Rev Biomed Eng* 11:109–134
- Taylor SH, Donald KW (1960) Circulatory studies at rest and during exercise in coarctation of the aorta before and after operation. *Br Heart J* 22:117–139
- Toprea BI, Schwarzacher SP, Chang A, Asvar C, Huie P, Sibley RK, Zarins CK (2000) Reduction of aortic wall motion inhibits hypertension-mediated experimental atherosclerosis. *Arterioscler Thromb Vasc Biol* 20:2127–2133
- Valentín A, Baek S, Humphrey J (2009) Complementary roles of vasoactivity and matrix turnover in arterial adaptations to altered flow, pressure, and axial stretch. *J R Soc Interface* 6:293–306
- Vignon-Clementel IE, Figueroa CA, Jansen KE, Taylor CA (2006) Outflow boundary conditions for three-dimensional finite element modeling of blood flow and pressure in arteries. *Comput Methods Appl Mech Eng* 195:3776–3796
- Wagner HP, Humphrey JD (2011) Differential passive and active biaxial mechanical behaviors of muscular and elastic arteries: basilar versus common carotid. *J Biomech Eng* 133(5):051009
- Weissler AM, Harris LC, White GD (1963) Left ventricular ejection time index in man. *J Appl Physiol* 18:919–923
- Whiting C, Jansen K (2001) A stabilized finite element method for the incompressible navier-stokes equations using a hierarchical basis. *Int J Numer Methods Fluids* 35:93–116
- Williams LR, Leggett RW (1989) Reference values for resting blood flow to organs of man. *Clin Phys Physiol Meas* 10(3):187–217
- Wilson N, Wang K, Dutton RW, Taylor CA (2001) A software framework for creating patient specific geometric models from medical imaging data for simulation based medical planning of vascular surgery. *Lect Notes Comput Sci* 2208:449–456
- Wolinsky H (1970) Response of the rat aortic media to hypertension. morphological and chemical studies. *Circ Res* 26(4):507–522
- Wolinsky H (1972) Long-term effects of hypertension on the rat aortic wall and their relation to concurrent aging changes. Morphological and chemical studies. *Circ Res* 30(3):301–309
- Xiong G, Figueroa CA, Xiao N, Taylor CA (2011) Simulation of blood flow in deformable vessels using subject-specific geometry and assigned variable mechanical wall properties. *Int J Numer Methods Biomed Eng* 27:1000–1016
- Xu C, Zarins CK, Bassiouny HS, Briggs WH, Reardon C, Glagov S (2000) Differential transmural distribution of gene expression for collagen types I and III proximal to aortic coarctation in the rabbit. *J Vasc Res* 37(3):170–182
- Zamir M, Sinclair P, Wonnacott TH (1992) Relation between diameter and flow in major branches of the arch of the aorta. *J Biomech* 25(11):1303–1310
- Zhang DP, Edwards E, Mei L, Rueckert D (2009) 4D Motion modeling of the coronary arteries from CT images for robotic assisted minimally invasive surgery. *Proc SPIE* 7259:72590X-1-8
- Zhou Y, Kassab GS, Molloy S (1999) On the design of the coronary arterial tree: a generalization of Murray's law. *Phys Med Biol* 44(12):2929–2945